UCLA
UCLA Previously Published Works

Title

Self-Aligning Rotational Latching Mechanisms: Optimal Geometry for Mechanical Robustness

Permalink

https://escholarship.org/uc/item/9xr4x0gf

Journal

Journal of Mechanisms and Robotics, 16(1)

ISSN

1942-4302

Authors

Fernandez, Gabriel I
Gessow, Samuel
Quan, Justin
et al.

Publication Date

2024

DOI

10.1115/1.4057073

Peer reviewed

eScholarship.org Powered by the California Digital Library
University of California

Self-Aligning Rotational Latching Mechanisms: Optimal Geometry for Mechanical Robustness

Gabriel I. Fernandez[*,†], **Samuel Gessow**[*,†], **Justin Quan**[*], **and Dennis W. Hong**[*]

Robotics and Mechanisms Laboratory (RoMeLa), Department of Mechanical and Aerospace Engineering
University of California Los Angeles, Los Angeles, California 90095, USA

In concurrent work, we introduced a novel robotic package delivery system LIMMS (Latching Intelligent Modular Mobility System). Each LIMMS end effector requires a small, lightweight latching mechanism for pre-manufactured containers, such as cardboard boxes. In order to effectively process a high volume of packages, aligning the latching mechanism quickly and reliably is critical. Instead of depending on highly accurate controllers for alignment, we propose a novel self-aligning rotational mechanism to increase the system's tolerance to misalignment. The radial latching design consists of evenly spaced blades that rotate into slots cut into the box. When misaligned, the blades contact the edges of the engagement slots, generating a self-correcting force that passively centers the blades with the slot pattern. This paper introduces a mathematical framework with closed form expressions to quantify error tolerance for for these mechanisms. Through our mathematical and optimization analyses, it is shown that a 2-blade design can tolerate a maximum misalignment of 3 times the radius to the blade tips, much larger than commonly used designs with 3 or more blade-like contacts. Our approach can be generalized for a class of rotational latching mechanisms with any number of blades. Utilizing this theory, a design process is laid out for developing an optimal self-aligning rotational latching mechanism given desired parameters and task constraints. With this methodology, we designed, manufactured, and verified the effectiveness of both 2-blade and 3-blade self-aligning in practical experiments.

Keywords Latch, Probability, Optimal, Design, Mechanism, Rotating, Self-Correct, Self-Align, Symmetric, Robust, Passive, Modular, Robot, Delivery, Logistics, Multi-Modal, Legged, Wheel, Lock, Package, Box, and Blades.

Nomenclature

$\alpha_1, \alpha_2, \alpha_3$ arc length between intersections, Fig. 6.
β_1, β_2 angle from sector edge to line through r', Fig. 6.
F_N, μ normal force and coefficient of friction, Fig. 5.
γ angle of blade tip about (r', θ), Sec. 4.

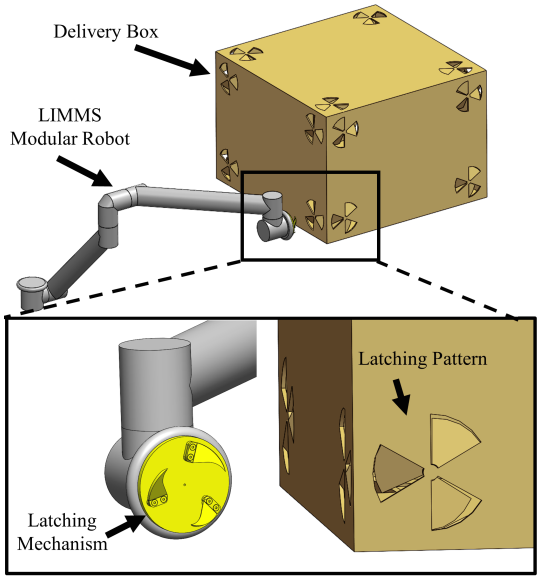

Fig. 1: LIMMS platform with a 3-blade latch design next to a delivery box with mating holes in the cardboard to be used as anchor points.

IC instant center, Fig. 5.
l_1, l_2 arc length of unblocked α_1 and α_2, Fig. 6.
p probability of latching success for a position, Sec. 4.
ϕ_1 half of the angle blocking the circle, Fig. 6.
ϕ_2 angle defined by ϕ_1 and blocking point, Fig. 6.
Ψ misalignment tolerance metric, Sec. 4.
r length from cutout center to nearest hole edge, Fig. 2.
r' length from assembly center to cutout center, Fig. 5.
R radial length of cutout, Sec. 4.
ρ length from blade assembly center to blade tips, Fig. 2.
τ torque applied to blade assembly center, Fig. 4.
θ angle between r' and nearest edge, Fig. 5.
ϑ angle between edges defining holes in pattern, Sec. 4.
V velocity, Fig. 5.
W length from blade assembly center to outer limit, Fig. 2.
x, y Cartesian coordinates of r and θ, Sec. 4.

Superscripts and Subscripts

* indicates an optimal parameter.
in, *out* refers to inner and outer alignments, respectively.
$|$ separates a functions inputs from given parameters.

[*]Corresponding authors: gabriel808@ucla.edu, sgessow@ucla.edu, justinquan@ucla.edu, and dennishong@ucla.edu.
[†]Equal contribution by the leading first two authors for this work.

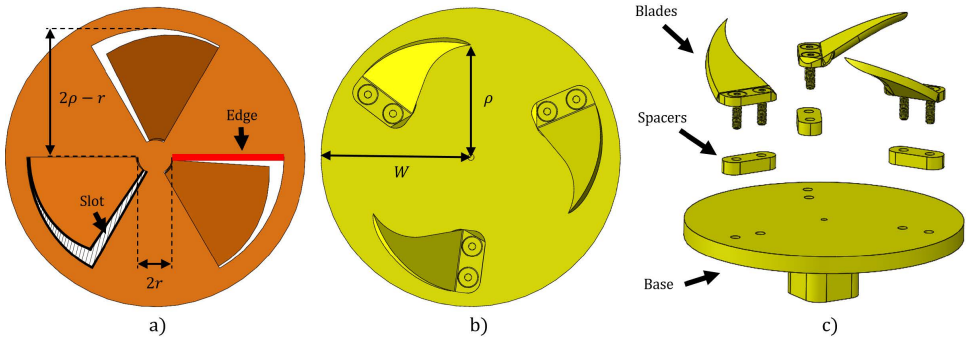

Fig. 2: a) Latching pattern cut from cardboard with red lines denoting engagement edges where the blades contact when fully engaged, b) Latch assembled configuration, and c) Components of the latch.

1 Introduction

To solve the last-mile delivery problem, we recently introduced LIMMS (Latching Intelligent Modular Mobility System) [1]. LIMMS is a novel decentralized robotic system that operates without a primary body. A single LIMMS unit resembles an appendage with latching mechanisms on both ends, which can serve as either the end effector or the base, as shown in Fig. 1. After securing one end to a fixed structure, the other end is free to behave like a manipulator or leg. For example, LIMMS could attach itself to anchor points on the surface of a wall to function as a manipulator, or four LIMMS latched to four corners of a box could walk like a quadruped, with the box itself serving as its body. Throughout the delivery process, LIMMS will have to frequently switch between walking and manipulating to process packages, which requires frequent latching and unlatching. Given the massive volume of packages shipped daily and the demand for faster delivery times, it is important to ensure that latching can happen quickly and reliably, or it can become a bottleneck that limits delivery times.

To perform its primary functions, LIMMS must be equipped with a latching mechanism that interfaces with both cardboard and wall-mounted anchor points integrated in delivery vehicles. Latching mechanisms for attaching and detaching components have been explored for a wide variety of applications, including tool changers [2], space vessel docking [3–5], and modular or self-configuring robotics [6–12]. The latching method varies widely depending on the use case, including spring-loaded pin locks, magnetic locks, and pneumatically actuated locks to constrain the parts in 6 DoF (degrees of freedom). In most cases, latching mechanisms rely on highly specialized gendered connectors with complex features to assist with alignment such as opposing grip claws [13], floating devices [14], and ball plungers [15].

While these examples offer good reliability and load support capabilities, they have distinct shortcomings that limit their applicability for our applications. Most latching mechanisms are bulky, heavy, or complex, requiring large geometric features for passive self-alignment or additional actuation to assist with alignment. They also have a small *area of acceptance* or range of possible starting conditions for which mating will be successful [16]. With a small range of alignment relative to their size, these mechanisms require precise positioning and orientation in 6 DoF during the docking process, making them slow to use.

Moreover, LIMMS has several operational restrictions that make conventional latching approaches unsuitable. First, the mating surface of the latching mechanism must be very cheap to integrate onto cardboard delivery boxes, since it is assumed that the box will be discarded after use. This means any additions to the box must have a small footprint and low mass to minimize production and delivery costs, respectively. Second, the mechanism should have a small volume and have minimal protruding features with mating surfaces in order to minimize the amount of volume lost in boxes and delivery vehicles. Finally, the mechanism's overall mass should be as small as possible, since excess weight at the LIMMS end effectors will negatively impact its load capacity and walking capabilities.

With these restrictions, the proposed solution is to integrate a female latching pattern on the cardboard delivery package. This involves cutting planar features and folding them out of plane to form flaps into the surface that can assist with alignment, depicted in Figs. 2, 4. This method results in a very low cost latching pattern for disposable cardboard. The male latch will be a lightweight radial design with blades that insert into the engagement holes with a twisting motion, which is easily generated by the wrist motor on LIMMS. This design passively aligns itself as it rotates, using contact forces from the pattern's geometry. The simple construction of this latching mechanism results in minimal mass added to the end effector. This proposed framework leverages geometry and mechanics for a self-aligning mechanism with maximum misalignment tolerance. By using radially symmetric patterns and point contacts for the blade tips, design parameters are chosen to have a higher chance of successfully latching given a position and random orientation around the axis of rotation. This minimizes time spent and control effort on alignment during delivery operations.

For our application, we formally derived the mechanics for self-aligning and its associated misalignment sensitivity for 3-blade and 2-blade latch designs with closed form expressions. From this, we formulated a metric associated with misalignment tolerance in the cardboard (X-Y) plane. By

choosing a desired tolerance, our mathematical models will calculate optimal design specifications for the latching mechanism and hole pattern. Our methodology is formulated in a general case so it may also be used for other applications.

The resulting LIMMS latch synthesized using these theories demonstrates superior alignment capabilities compared to existing 6-DoF latching and alignment methods. The underlying theory demonstrates the importance of certain factors for passive alignment that are not immediately apparent, which may be useful even for non-rotational latch designs. While most latches utilize 4 or more interfacing bodies (such as hooks, pins, blades, etc.), our models show that reducing the number of constraints at the interface makes successful alignment easier. Since each body takes up space and can overconstrain the latch, we found that the 2-blade design was generally favorable for alignment. The following summarizes our contributions in this paper:

1. Introduced a class of self-aligning mechanisms,
2. Characterized their mechanics and likelihood of misalignment for the 2-blade and 3-blade designs,
3. Formulated an error tolerance metric by which optimal design specifications can be determined, and
4. Verified results in simulation and hardware.

2 Problem Setup

The mechanism presented in this paper can be viewed independently from any specific application. Thus, our method can be formulated to address a class of self-aligning rotational latches. The generalized problem can be constructed with the following criteria:

- Self-alignment at a fixed position is unique up to a finite number of rotational symmetries,
- Actuation only occurs about the latch's axis of rotation,
- Design parameters should be optimal with respect to any two of the following constraints: space, strength of mating surface material, and error tolerance.

The last point on design parameters comes from the design process proposed in Sec. 5 and derived through our analyses in Sec. 4. We show that by choosing any two of the design parameters with respect to the total workspace of the latch W, strength of the center island of the pattern r, which is dependent on the strength of the material, and misalignment tolerance metric Ψ, optimal parameters are fully defined.

For this paper, the female component with cut engagement slots will be referred to as the *hole pattern* (Fig. 2a) and the male component as the *latch* (Fig. 2b) with equally spaced blades. The scope of this paper only covers self-alignment and deriving optimal designs for the latch and the cut hole pattern geometries. Other areas of interest, such as locking the assembly in place, blade angle of attack, speed, and load distribution will be considered in future work.

Assumptions The majority of our mathematical and geometric derivations rely on a few basic assumptions:

- A counter-clockwise torque is used for latching.
- Slots cut into the latching pattern are radially symmetric pieces of a circle as shown in Fig. 2 with colinear edges extending to R. There is an *island*, the non-hole portion at the pattern center as seen in Fig. 2a with radius r.
- The latch face and the surface of the latching pattern are always parallel with one another and interact primarily in a plane, and out-of-plane effects are minimal. However, this assumption is not strictly required, as shown during the hardware testing in Sec. 5. These tests show that the mechanism could tolerate out-of-plane misalignment and could still perform successful self-alignment when angled slightly from parallel. Please see the video link in footnote[1].
- The forces applied to the latching mechanism in the X and Y directions (parallel to the latch surfaces) during engagement are minimal. This assumption, however, is also not strict as shown during hardware testing where the robotic arm does apply forces in X and Y, see video[1].

Several assumptions were made about the physical behavior of the latch as the blades interact with the pattern's cut slots. It is assumed that the blades slide along the card-

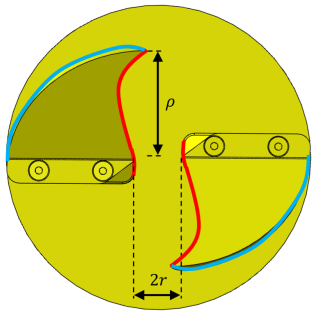

Fig. 3: Two blade design showing inner (red) and outer (blue) edges that correspond to inner and outer alignment methods.

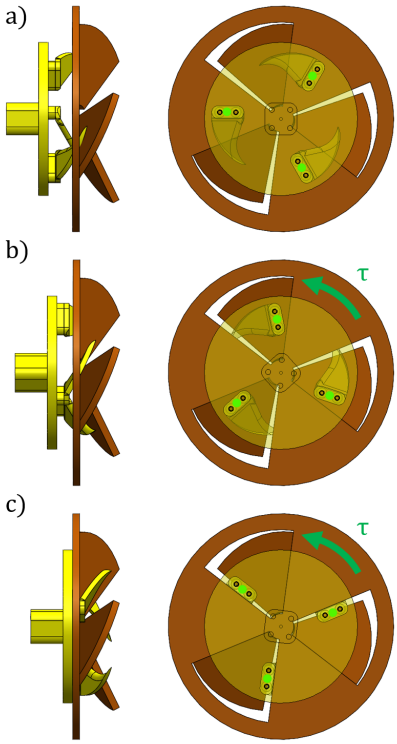

Fig. 4: Shows a sequence of a three blade design spinning to align.

board pattern's surface and fall into the engagement slots, ultimately resulting in a line of contact between the slot's engagement edge and the blade spacers, shown in red in Fig. 2. Thus, it is also assumed that the shape of the slot itself ultimately does not matter for final engagement, other than the red engagement edges. These edges are radially symmetric intersecting at the center. For the 3-blade design, it is kinematically impossible to be greater than one latch radius away, since being greater than one radius away would result in one of the blades being constrained to the same hole or outside of the hole pattern region.

Due to these assumptions, in addition to this kinematic constraint, full cutouts for the 3-blade are not drawn and are instead treated as a line as seen in Fig. 5, 6. This lack of dependence on overall slot shape is verified in practical testing. However, this is not the case for the 2-blade design. In [17] we used a conservative model for the 2-blade latching where only the final alignment edges when the blade is fully engaged were considered. We extend this to include all edges.

Furthermore, we make the assumption that there is minimal penetration into the hole pattern. Additionally, once a blade is inside a hole pattern it is constrained to be within a hole pattern. Including these two assumptions gives us a more realistic model and surprisingly substantially increases the total probability as seen in Sec. 4. Again, this phenomenon is not seen in the 3-blade assembly due to it being kinematically overconstrained.

In Sec. 2 derivations, it is assumed that the blade's radial location can be approximated as a single point, depicted by green dots in Fig. 4, 5. In the case of three or more blades, the blade spacer and the engagement edge will only contact at a single point until the latch is fully engaged due to the spacer's rounded shape. Additionally, the width of the spacer can be ignored since the blades have a triangular shape. If the blades are rotated off-center, the sloped surfaces of the blade will contact the pattern edges and force its overall location to adjust until it's aligned with the blade's tip. We tested a mechanism with three pins to verify that this assumption is valid as seen in the supplementary video[1].

In later derivations for Sec. 4, it is assumed that the shape of the blade does not matter beyond the requirements laid out in Sec. 2. For this reason only the point locations of the blade tips and where they start are considered.

In all derivations, the mating pattern surface is assumed to be much stiffer than the forces it is subjected to. This assumption needs verification based on the application and materials involved. In our case, the cardboard's strength is high enough for this assumption to be valid.

Finally, only the 2-blade and 3-blade cases for the latch were considered. Preliminary analyses showed that for more than three blades, the error tolerance is worse, and there are no additional benefits. For successful alignment, each blade must start its rotation in a separate angular region, since two blades cannot enter the same engagement slot. Since blades must be evenly spaced over 2π rads, increasing the number of blades effectively decreases the angular region available for each blade to start at for successful alignment. Also, a single blade latch is not able to meet the self-aligning requirements as it cannot both constrain the angle and the position of alignment when radially inserted into the mating surface.

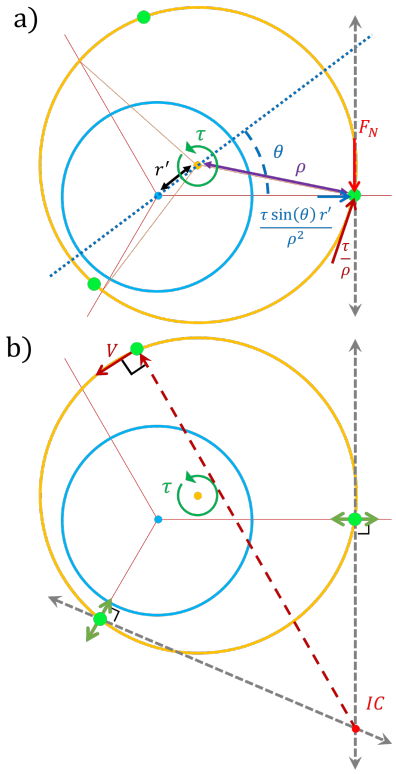

Fig. 5: Visual representation of 3 blades (bright green dots on orange circle) aligning with the hole pattern center island (blue circle). a) First, a single blade engages the cutout edge (red) shown by the green dot on the far right. b) A second blade engages, resulting in a V in the direction of alignment. The dark green arrows depict the edge of constraint in which the blades can move given the torque direction.

3 Alignment Mechanics

The next section analyzes the mechanism's sequence of operations and self-aligning motion when the latch is actuated to rotate about its center. For this analysis, it is assumed that the starting configuration for latching is with the blades lightly pressed against the surface of the cut pattern at some initial position (r', θ) and angle of rotation about the latch's center axis γ similar to the configuration in Fig. 4a.

3.1 Alignment with Two Blades

The 2-blade latch design consists of blades with an angular separation of π rads as shown in Fig. 3. As the two blades rotate and travel along the surface of the cut pattern, the first blade that contacts the pattern's edge becomes the new pivot point that the latch begins to rotate about.

Once the second blade engages with an edge in the opposing hole, the latch moves along the two aligned edges at the latch's centerline. With only two blades, it would appear impossible to fully constrain the position and rotation, r' and θ, given only a rotational actuation about its center. However, the final constraint needed for a self-correcting motion

[1] Experiments, verification, and a brief explanation of this paper can be found online at: https://youtu.be/W5_3vF3nT28

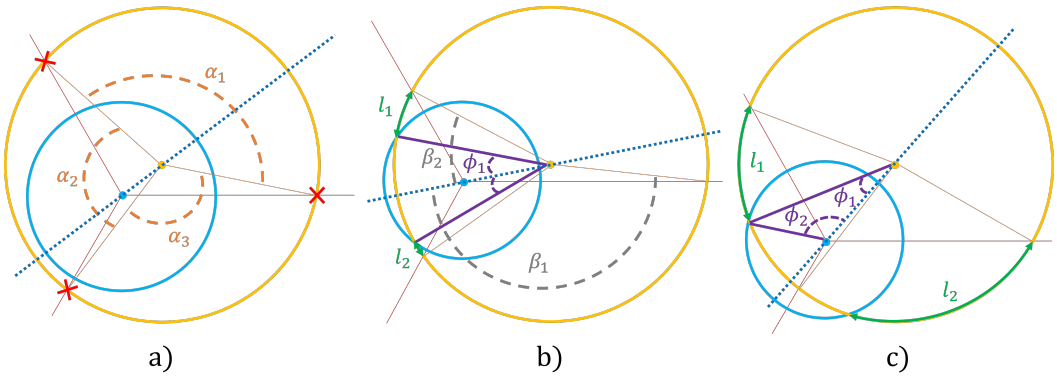

Fig. 6: The 3 alignment cases for the 3-blade design: a) Case 1 where there are no intersections, b) Case 2 where both intersections are either completely in α_2 or α_3, and c) Case 3 where one intersection is in α_2 and the other is in α_3.

comes from the blade profiles as the latch inserts its blades further into the the pattern.

This self-correcting motion comes from the contact force between the blade and the engagement edge as it rotates. This contact can occur at the blade's inner edge or outer edge. When the inner edge of the blade presses into the center island of the hole pattern, this is referred to as *inner alignment*, with the inner edge depicted in red in Fig. 3. *Outer alignment* is when the blade edge furthest from the center pushes on the outer edges of the hole during engagement, depicted with the blue edge in Fig. 3. As the latch continues to rotate, self-alignment occurs until the faces of the latch and hole pattern are touching. The latch then becomes fully constrained due to the width of the blade.

Inner Alignment Since inner alignment uses the inner edge of the blade, the blade needs to taper from its maximum allowable distance from the center W at the tip of its blade to r. Let $f(t)$ describe the inner edge contour, with $f(0) = (\rho, \theta)$ and $f(1) = (r, 0)$. As long as this contour follows the property that $||f(t)||$ is monotonically decreasing, then alignment will be successfully achieved.

Outer Alignment For outer alignment, no center island is needed, and the blade uses its outer edge of the hole pattern to align. In this case, the blade tapers out from its minimum distance from the center ρ at the blade's tip to W when fully aligned. This contour has a $f(t)$ where $f(0) = (\rho, \theta)$ and $f(1) = (W, 0)$. If the contour obeys the property that $||f(t)||$ is monotonically increasing, then alignment will succeed.

3.2 Alignment with Three Blades

The process of aligning with 3 blades can be broken down into four stages: no blade engaged, then one engaged, followed by two, and then finally all three. Note that it is not required to start at the first stage, although it is the most likely case. The blade locations are modeled as points, shown in green in Fig. 4, 5 and mentioned in Sec. 2.

The behavior of the first 2 stages closely follow the mechanics for the 2-blade case, where the first blade that contacts the edge of an engagement pattern becomes the new pivot point that the latch begins to rotate around. The behavior of this pivot point and the direction of velocity can be explicitly stated using instant centers, IC.

From the starting configuration, the mechanism first spins until one point makes contact with an edge. As torque τ is continued to be applied, the resulting forces can be seen in Fig. 5a. The figure further shows that the IC is not fully constrained since there is only one line (dotted grey) perpendicular to hole pattern edge (red line). In other words, the IC would need another grey dotted line that intersects to define a fully constrained point. Assuming $\mu F_N \geq \frac{\tau \sin\theta r'}{\rho^2}$, the far right green dot in Fig. 5a will be a stationary point, making it the IC. The blade assembly (large orange circle) rotates like a wheel around that point until the blade (green dot) contacts with the second edge. Even if slipping occurs, the constraint line (dark green) would cause the IC to be on the grey line, which would lead to the second point engaging (green dot).

Once two points are in contact, the points are only free to slide along the edge of the cutouts as shown in Fig. 5b. The IC for these two velocities appear in the lower right of the figure indicated by a red dot. The direction of the resulting velocity V is perpendicular to the line through the IC. This will continue until the third and final blade engages.

Finally, the three points provide three independent constraints, fully defining the latch's position and orientation given the axis of rotation and direction of τ. In this state the F_N from the edges are equal and opposite to those caused from τ, so the latching mechanism cannot move and is fully constrained at the target alignment.

4 Alignment Tolerance Analysis

One of the key features of our latching mechanism is its robustness to misalignment. Given an initial position (x, y) or (r', θ) in polar, and a random orientation γ of the blade assembly about its center axis, a probability distribution over the area of the cutout mating surface can be derived. In [17] we demonstrated the superiority of the 2-blade latch by comparing a conservative model of its probability distribution of latching successfully with that of the 3-blade latching mechanism in closed form. As an extension of [17], we include all four edges as show in Fig. 8a that fully define a hole in the pattern. In addition in contrast with our previous analysis we highlight the importance of ϑ, the angle from which

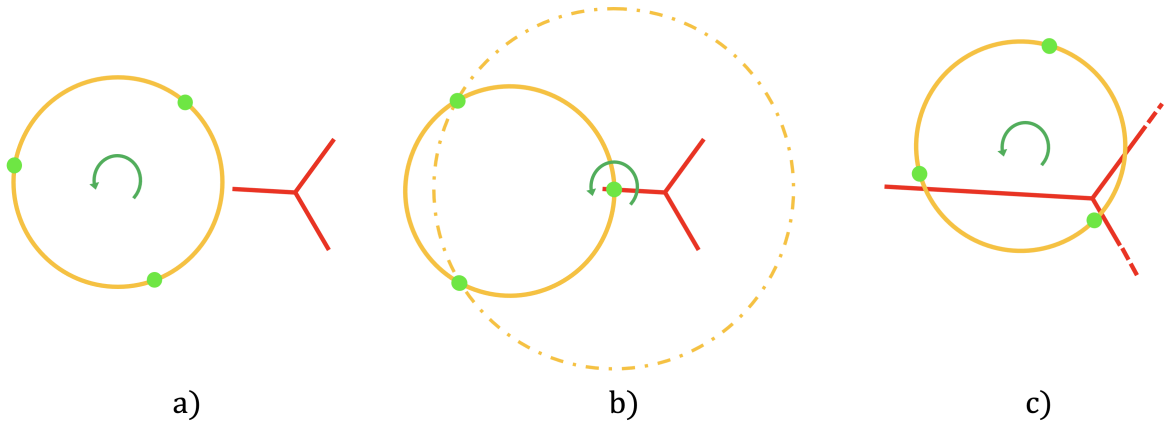

Fig. 7: Failure types: a) Type 0 where no edges engage with the pattern, b) Type 1 where a single blade engages but the resulting trajectory causes the other blades to spin outside of the pattern, and c) Type 2 where 2 blades end up in the same region or 2 blades constrain the latch to a failure case.

the edges expand radially. In the 3-blade case the probability distributions stay the same as it cannot take advantage of the edge defined by the outer arc, since it would simply be constrained to only failure cases. However, the 2-blade case does not have this issue, and its overall probability drastically increases. In this section we first prove that a set of optimal parameters exist and show how to obtain them for the 2-blade case. Then we show how suboptimal parameter choices can affect the probability distribution. Finally, the derivations for the probability distributions for the 3-blade design are used to draw contrast to the robustness of the 2-blade design.

To draw a fair comparison between inner and outer alignment the maximum area for the latch is defined by radius W, island size r, pattern angle by ϑ, and the integral of the probability distribution for successfully latching. Successfully latching means that each blade engages edges within different holes of the pattern. The number of failure modes varies based on parameter choices. The types of failure modes are defined as follows:

- Type 0: No blades engage with any edge,
- Type 1: One blade engages with one edge, while the other cannot engage with any edge, and
- Type 2: Two blades engage edges within the same hole.

4.1 Two Blades

The probability distribution for the 2-blade design depends on certain parameters for both the pattern and the latch. The pattern is defined by r, R, and ϑ, and the blades are defined by ρ and W. The parameters ρ^*, R^*, and ϑ^* can be converted to only depend on r^* and W^*. In this section the optimal parameters for 2-blade inner align are derived for R^* in a bounded set. Outer align derivations follow similarly.

4.2 Inner Align

Proposition 4.1. *For 2-blade inner align:* $\rho^* = W^*$.

Proof. By definition of W it follows: $\rho \not> W \ \forall \ \rho, W$. Therefore, we consider if $\rho < W$. There exists some scaling between R and ρ such that simply increasing both by this factor would increase the overall maximum area of successfully latching and the total probability mass. Therefore, $\rho^* = W$ and vice versa following the same logic for W^*. □

Lemma 4.1. *For 2-blade inner align:* $R^* \in [2\rho - r, \sqrt{\frac{1}{2}(r^2\cos 2\vartheta - r^2) + 4\rho^2} - r(\cos\vartheta - 1) - r]$.

Proof. If $R < 2\rho - r$, then simply increasing R increases the total probability of successfully latching. As R increases the number of Type 0 failures strictly decreases since the maximum distance of engaging an edge increases. Some Type 0 failures get converted to Type 1 assuming small enough R. As R increases, Type 1 failures strictly convert to successes. Type 2 failures cannot exist in this case since $2\rho \gg R$ and the blades' circular trajectory cannot fit within the pattern.

The upper limit $\sqrt{\frac{1}{2}(r^2\cos 2\vartheta - r^2) + 4\rho^2} - r(\cos\vartheta - 1) - r$ is the furthest distance away an engagement point can be in order to successfully latch as seen in Fig. 8b. This point is defined by the furthest corner of a hole and the corresponding nearest small corner of the opposing hole. This distance at most is 2ρ. This is then used to calculate the theoretical upper bound. If $R > \sqrt{\frac{1}{2}(r^2\cos 2\vartheta - r^2) + 4\rho^2} - r(\cos\vartheta - 1) - r$, one blade engaging on any part of the larger arc of the hole pattern, as seen in Fig. 8a, will result in a Type 1 failure since it can no longer reach the other hole. Decreasing R would serve to reduce those Type 1 failures. □

For our purposes, we define R^* as the following: $\widehat{R}^* = 2\rho - r$, where $\widehat{R}^*$ is a close approximation with bounded error on the true R^*. When $r = 0$, $R^* = \widehat{R}^*$ since it is independent of ϑ and r. Furthermore, since $\widehat{R}^*$ is the lower bound on R^*, the probability distribution for one half of the hole pattern (since it's rotationally symmetric by π) is a convex hull. This property provides continuous area without any break near the center as seen in Fig. 9a. From a controls perspective having any low probability around or near the axis of pattern engagement would be detrimental.

Lemma 4.2. *For* $r \in (0, \rho)$, $\vartheta^* \in (\frac{\pi}{3}, \pi)$. *As* $r \to 0$, $\vartheta^* \to \frac{\pi}{3}$.

Proof. First, we establish that the largest distance between any two points on the edges of a single hole d: $d = 2\rho \implies \exists\vartheta^*$. If $d > 2\rho$, Type 2 failures strictly increase since there now is a length in which two blades can fit into the same

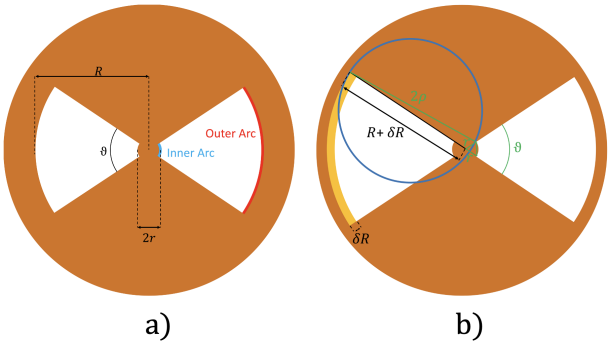

Fig. 8: a) Diagram showing all the parameters that define the latching pattern for the two blade case. b) $R+\delta R$ indicates the maximum length that R can be. The features in green are used to calculate the length.

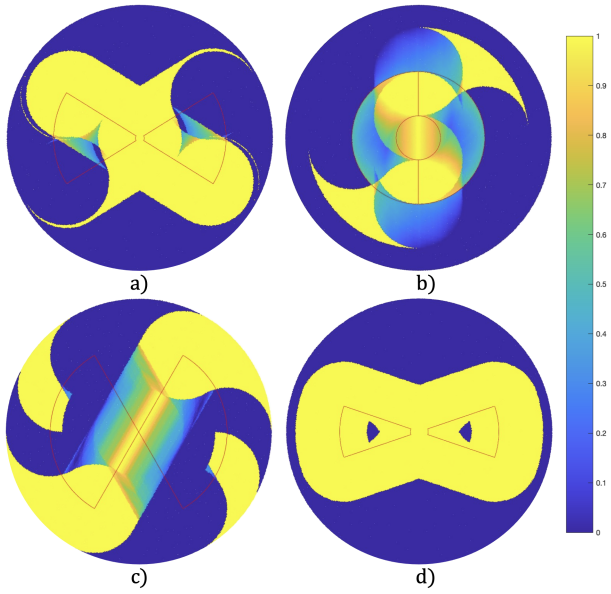

Fig. 9: a) Probability distribution when R is bigger than the upper bound from Lemma 4.1. b) Probability distribution when ϑ is almost π. c) Probability distribution when $r=0$ and $\vartheta=\frac{2\pi}{3}$. The area of high probability is mostly out to the corners, which is not ideal for controllers. d) Simulation showing how the probability distribution decreases when $\vartheta<\vartheta^*$.

hole. As d increases more successes are converted to Type 2 failures. Similarly, if $d<2\rho$, the number of Type 0 and Type 1 failures strictly increase since the trajectory of a latch can either completely encompass one of the hole patterns or engage with one hole pattern and encircle the other without making contact. At $d=2\rho$, with probability zero it will be in an initial condition where it fails, since there are only single points of failure along a continuous spectrum of real numbers. Therefore, $d=2\rho$ is a necessary condition for the optimality for ϑ^*.

If $r=0$, then $\widehat{R}^*=2\rho$ by definition. Then the longest length $d=2\rho$. That means $\vartheta\in(0,\frac{\pi}{3})$ and is not unique. We take ϑ^* to be the maximum value since increasing ϑ increases the overall potential to convert Type 0 and Type 1 failures to successes as the total area has increased, meaning $\vartheta^*=\frac{\pi}{3}$ from it being an isosceles triangle. The other bounds are its physical limits by definition. □

Theorem 4.3. *There exists a unique ϑ^* for every $\widehat{R}^*$, and ϑ^* is monotonically increasing with respect to r:*
$\exists!\ \vartheta^* \quad \forall\, \widehat{R}^*,\ r\in(0,\rho)$.

Proof. From Lemma 4.2, when $r=0$, ϑ^* is chosen to be as large as possible to increase the total number of potential successes. The argument for the remaining interval of r follows similarly to the analysis presented in Lemma 4.1.

For $\vartheta<\vartheta^*$, then $d\leq 2\rho$ where the total number of failures either decrease or remain the same when ϑ is increased. Type 0 failures decrease as the area of the hole is larger. Type 1 failures remain unchanged or decrease since the possible number of intersections in opposing holes have increased. There will still be no change in Type 2 failures as $d\leq 2\rho$ except for potentially a few instances with zero probability. A probability distribution for this case is shown in Fig. 9d.

Now that ϑ is monotonically increasing in r and is unique, we show that this definition is optimal. For $\vartheta>\vartheta^*$ the overall probability distribution decreases. By adding a small angle, $\delta\vartheta$ to ϑ^* as shown in Fig. 13. We can analyze what happens when $\vartheta>\vartheta^*$. To complete this proof, a key insight was that adding δr introduced a half circle of probabilities centered at δr that changed from 1 to 0 as shown in Fig. 13. At the same time, adding $\delta\vartheta$ will convert part of a radius of probability from 0 to 1. An under-approximation of the probability loss δP_l and over-approximation of the probability gained δP_g are as follows:

$$\delta P_l = \delta r\pi\rho$$
$$\delta P_g = \frac{(2\rho)^2}{2}\delta\vartheta - \frac{r^2}{2}\delta\vartheta\ .$$

These regions are shown in Fig. 13b. The derivation of these equations is provided in Appendix 6. Based on this insight the relationship between $\delta\vartheta$ and δr is critical and defined as:

$$\delta r = \frac{2\rho sin(\delta\vartheta)}{2sin(\delta\vartheta+\vartheta)}\ .$$

Using this relationship we find:

$$\delta P \leq 2\delta\vartheta\rho^2 - \frac{\delta\vartheta r^2}{2} - \frac{4\delta\vartheta\rho^2\pi}{2\delta\vartheta+\vartheta}\ .$$

The right-hand side of this equation is negative over the following sets of parameters defined by physical limitations:

$$\{r,\rho,R|0\leq r<\rho\leq R\leq 1\}$$
$$\{\vartheta,\ \delta\vartheta\ |0<\vartheta<\pi,\ 0<\delta\vartheta<(\pi-\vartheta)\}\ .$$

Now when substituting the appropriate upper bounds to maximize the right-hand side, we prove it is always negative on these sets:

$$2\delta\vartheta\rho^2 - \frac{4\delta\vartheta\rho^2\pi}{2\delta\vartheta+\vartheta} \qquad \text{(Substitute minimum } r\text{)}$$
$$2 - \frac{4\pi}{2\delta\vartheta+\vartheta} \qquad \text{(Factor out } \delta\vartheta \text{ and } \rho^2\text{)}$$
$$2 - \frac{4\pi}{2\pi-\vartheta} \qquad \text{(Substitute maximum } \delta\vartheta\text{)}$$
$$2 - \frac{4}{2-\varepsilon} \qquad \text{(Substitute } \varepsilon\pi>0 \text{ for } \vartheta\text{)}$$
$$2 - \frac{4}{2-\varepsilon} < 0\ , \qquad \forall\,\varepsilon\in(0,1)\ \text{(Bounds on } \vartheta\text{)}\ .$$

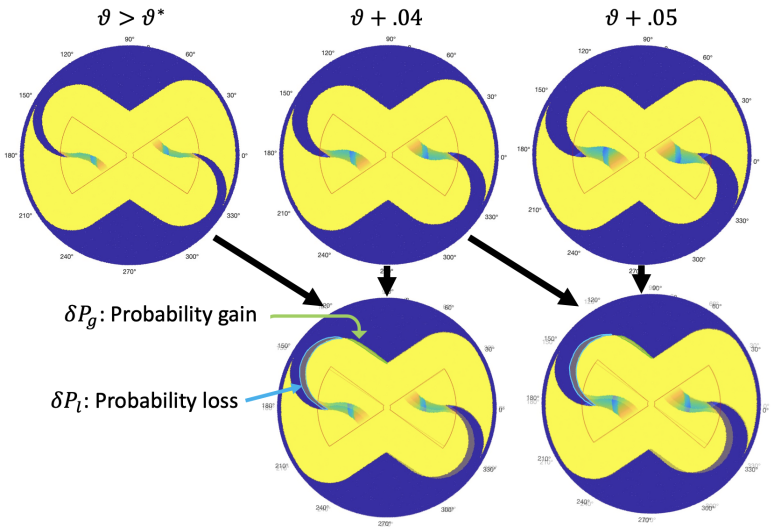

Fig. 10: Simulations showing a progression of increasing ϑ. Note how when they are overlaid the regions described in Theorem 4.3 show up.

In addition, there is also a similar line of decreased probability for an arc-like area centered about the bottom corner of the pattern. It is also caused by an increase in the likelihood of Type 2 failures. This line, however, does not add areas of zero probability, as there are still starting angles that lead to successful alignments due to the rotation direction of the latch. This covers where δr increases with $\delta\vartheta$.

Once ϑ is sufficiently large, increasing $\delta\vartheta$ cannot increase δr, as the entire upper edge of the slot already results in failure. In this case, no new area is gained or lost on the upper edge or half circle around the upper corner, but the area around the lower corner still decreases as the likelihood of Type 2 failures is still increasing. Therefore, the change in probability brought about by a change in angle from ϑ to $\vartheta + \delta\vartheta$ is always negative.

Intuition In Fig. 10, $\delta\vartheta$ is much larger than the one used in the argument for visualization purposes, which results in regions being shaped slightly differently. However, the regions of interest and arguments still follow.

The final piece of the argument relies on the independence of $\hat{R}^*$ and ϑ^*. To see this we superimposed two distributions, one with a suboptimal R and another with a suboptimal ϑ in Fig. 11. By rotating the superimposed image of the hole pattern of suboptimal R over the hole pattern of suboptimal ϑ, the overlapping regions compose to form the combined suboptimal R and ϑ graph. □

We found the approximation of R^* with $\widehat{R}^*$ for inner align did not affect performance noticeably in our practical experiments in Sec. 5. We consider deriving the exact R^* to be outside the scope of this paper and will derive the exact solution in future work.

4.3 Outer Align

The propositions, lemmas, and theorems from the previous inner align section also apply to outer align. The arguments are the same in both cases since the model has been simplified down to contact points kinematically interacting with edges. The only difference is W because the outer align uses the outer edges to self-align and, therefore, will be larger than ρ. Additionally, as a design principle, r is always 0 for outer alignment. This is because r arises from a mechanical constraint dictated by the material and application. Since outer alignment uses the outer edge, it does not need any strength for the center island. In fact, having a center island creates an additional constraint, resulting in an adverse effect. Even if r is small, assuming the island can hold, one should just use inner align and scale the latch and pattern for the same W. Therefore, for outer align $r = 0$ is the only case considered.

Lemma 4.4. *For outer alignment $R^* = W$, and $\rho^* = \frac{R}{2}$.*

Proof. By definition to fully constrain the latch using outer align: $R = W$. If $R > W$, the latch cannot be fully constrained with the pattern. If $R < W$, there is more than one way to be constrained. Therefore, $R^* = W$ to uniquely constrain the alignment of the latch and pattern. By following the proof Lemma 4.1 with $r = 0$, the bounds converge to a single point $\rho* = \frac{R}{2}$, implying $R^* = 2\rho$. □

Unlike in the inner align case, we can derive the optimal set of parameters without approximating R^*. Since kinematically, the analysis of outer align follow exactly the same as the inner align section above but instead of $\widehat{R}^*$ being used the true R^* is used. We now can claim that these are the exact optimal parameters for outer align.

Theorem 4.5. *For outer align, the summation over the probability distribution for ϑ^* and R^* is greatest for a given ρ when $r = 0$.*

Proof. By Lemma 4.1

$$P(\vartheta \neq \vartheta^*, R \neq R^* | r, \rho, W) < P(\vartheta \neq \vartheta^*, R^* | r, \rho, W)$$

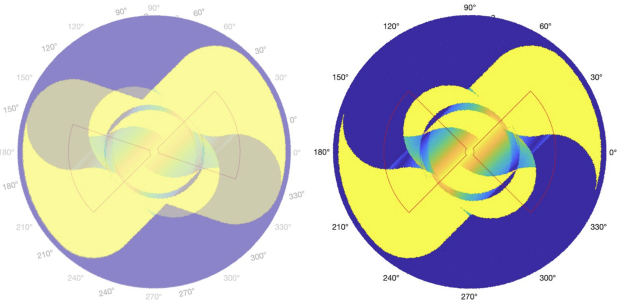

a) b)

Fig. 11: a) Independent probability distributions suboptimal R and suboptimal ϑ overlaid. Red hole pattern is of suboptimal R. The hole pattern for suboptimal ϑ is the same as the figure on the right. b) Probability distribution for combined suboptimal R and suboptimal ϑ. By rotating the superimposed hole pattern of suboptimal R over suboptimal ϑ from the graph on the left, the overlapping regions compose to make the figure on the right.

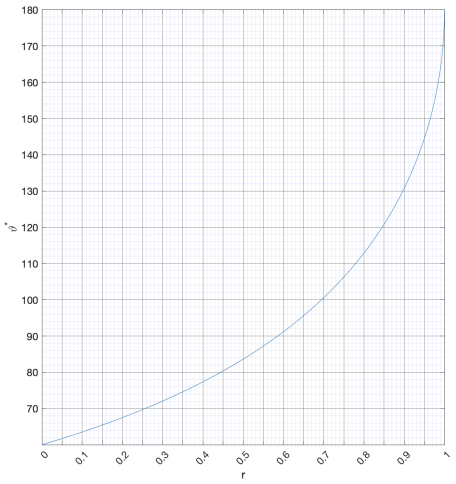

Fig. 12: Optimal value of ϑ^* for a given island size r.

And by Lemma 4.3

$$P(\vartheta \neq \vartheta^*, R^* | r, \rho, W) < P(\vartheta^*, R^* | r, \rho, W)$$

Therefore, the probability is the greatest for ϑ^* and R^*. □

Now that we have proved optimal parameters, we derive the probability distribution for those parameters. These distributions shown in Fig. 15 are calculated by taking points ρ away from the edge of the hole pattern.

4.4 Three Blades

For the 3-blade case, the blades must be evenly spaced for radial symmetry, so they must be located $\frac{2}{3}\pi$ apart. These probabilities are rotationally symmetric. In order to achieve successful latching in the 3-blade case, each blade needs to start in separate regions outlined in Fig. 5, 6 and not be blocked by the center island. This is because each blade must be able to enter an engagement slot after rotating, and no two blades can physically enter the same slot. If the center of the latch is positioned such that an orientation exists where each blade is located within its own region (and will enter its own slot), then a non-zero probability exists that latching will succeed. If the probability distribution is defined over a single region, it can be rotated by $\frac{2}{3}\pi$ to get the full distribution.

The boundary with zero probability for a single region, i.e., $0 \leq \theta < \frac{2\pi}{3}$, is defined. For latching to be possible, when one blade is engaged and the assembly begins to rotate, the second blade must be able to reach the other side of the island to engage: $|r'| \leq \rho$.

Two additional constraints appear due to the center island area blocking any blades from entering the engagement slots, which would also result in zero probability. Fig. 6b, c show how the center island creates new boundary constraints given by: $y^2 + (x-r)^2 \leq \rho^2$ and $(y - r\sin(\frac{2\pi}{3}))^2 + (x - r\cos(\frac{2\pi}{3}))^2 \leq \rho^2$.

Case 1 $|r'|$ is sufficiently small such that the trajectory of rotation about the blade assembly's center, shown in orange in Fig. 6a, does not intersect the center island indicated by the blue circle. In this case, the arc length of interest is the smaller of α_2 and α_3, since it defines the first blade to violate a boundary. However, there are also blades located $\frac{2}{3}\pi$ away in the other regions. The feasible arc lengths of these blades need to be considered as well. The minimum of this is divided by $\frac{2}{3}\pi$ to give the probability.

Case 2 The trajectory when rotating about the assembly's center intersects the center island exactly twice as seen in Fig. 6b, c. Depending on where the intersection occurs, the probability distribution function $p(\cdot)$ varies. If the intersections are both in the same region, then it would look similar to Fig. 6b. In this scenario, the arc lengths of l_1 and l_2 are of interest, as well as how much of the other region is available for the blade tip, which is $\frac{2}{3}\pi$ away engaging. This is done for both l_1 and l_2, always taking the minimum of it and its offset. Once this is done all of the resulting arc lengths are summed and divided by $\frac{2}{3}\pi$ to give the probability.

Case 3 The intersections are split across sectors as shown in Fig. 6c. This case is similar to Case 1 where there are no intersections. The only exception is when α_2 and α_3 are blocked by the center island.

The probability function for the 3-blade case is not continuous since it must take into account different cases and take minimum values. In order to present the closed form expression of p, several intermediate variables are provided to simplify the expression, also depicted in Fig. 6:

$$\beta_1 = \frac{\pi}{3} - sin^{-1}\left(\frac{r'\sin(\theta)}{\rho}\right) - \theta$$

$$\beta_2 = \frac{\pi}{3} - \sin^{-1}\left(\frac{r'}{\rho\sin(\frac{2\pi}{3} - \theta)}\right) + \theta$$

$$\beta_3 = \frac{\pi}{3} - sin^{-1}\left(\frac{r'\sin(\frac{2\pi}{3} + \theta)}{\rho}\right) - \theta$$

$$\alpha_1 = (2\pi - (\beta_2 + \beta_1))$$

$$\alpha_2 = \beta_3 + \beta_2.$$

For 3 blades p is as follows:

Case 1: $r' \leq \rho - r$ (0 or 1 intersections with the island)
$p = \min(\alpha_2 + \alpha_3 - \frac{2\pi}{3}, \min(\alpha_2, \alpha_3))$

Case 2: $r' > \rho - r$ (2 intersections with the island)

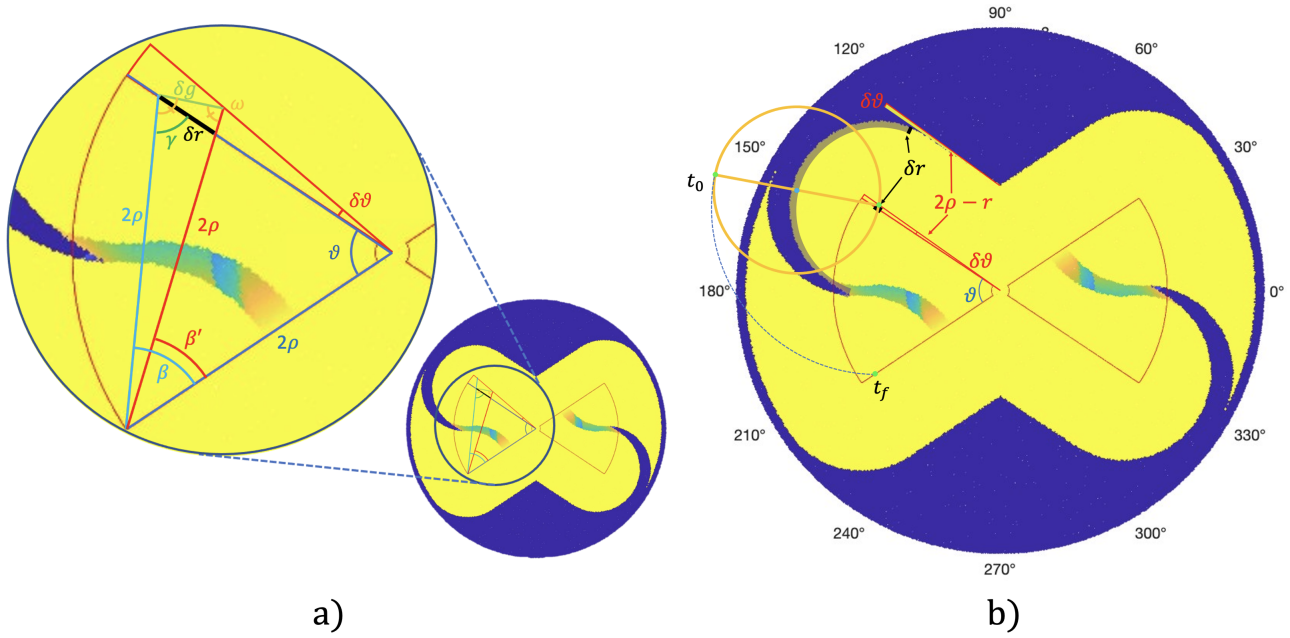

Fig. 13: a) Geometry used for relating $\delta\vartheta$ to δr. The red line with angle B' and the blue line with angle β is defined to have length of 2ρ. b) By perturbing ϑ^* by $\delta\vartheta$, a net loss of probability mass occurs, despite an overestimation of the probability gained, shown by the little triangle sticking out on the upper left of the probability defined by $\delta\vartheta$ and $2\rho - r$, and an underestimation of the probability loss, shown by the greyed out yellow arc in the upper left.

(a) $\theta - \phi_2 < \frac{4\pi}{3}$ (2 intersections in α_2)
$l_1 = \beta_2 - \phi_1$
$l_2 = \beta_1 - \alpha_3 - \phi_1$
$p_1 = \min(\max(\alpha_2 + \alpha_3 - \frac{2\pi}{3}, 0), l_1)$
$p_2 = \min(\max(\alpha_2 + \alpha_3 - l_1 - 2\phi_1 - \frac{2\pi}{3}, 0), l_2)$
$p = p_1 + p_2$

(b) $\theta + \phi_2 > \frac{4\pi}{3}$ (2 intersections in α_3)
$p_1 = \min(\max(\alpha_2 + \alpha_3 - \frac{2\pi}{3}, 0), l_1)$
$p_2 = \min(\max(\alpha_2 + \alpha_3 - \frac{2\pi}{3} - l_1 - 2\phi_1, 0), l_2)$
$p = p_1 + p_2$

Case 3: $r' > \rho - r$ (1 intersection in α_2 & other in α_3)
$\theta + \phi_2 \leq \frac{4\pi}{3}$ and $\theta - \phi_2 \geq \frac{4\pi}{3}$
$p_1 = \max(\min(l_1, l_2) + 2\phi_1 - \frac{2\pi}{3}, 0)$
$p_2 = \min(\alpha_2 + \alpha_3 - \frac{2\pi}{3}, \min(l_1, l_2))$
$p = \max(p_2 - p_1, 0)$

4.5 Alignment Tolerance Metric Ψ

With probability p now defined, the performance of different latch designs can be compared based on their alignment tolerance. Ψ is a scalar quantity that can help compare relative designs by summing over p:

$$\Psi(W, \rho, r) = \int_{D(0, Wc)} p(r', \theta | r, \rho, W) dA \qquad (1)$$

where $p(r', \theta | r, \rho, W)$ is defined above, and c is a constant based on the application. It is constrained to $c \leq 3$, as this will capture the entire distribution. Due to the complexity and piece-wise nature of p, Ψ can most easily be computed numerically. Ψ is not unitless to allow it to maintain a physical meaning for design comparisons. Comparisons are made on a relative scale for similar designs, but there are nuanced specifications in which looking at both p and Ψ could be even more beneficial.

The best case offset from the center comes from the 2-blade case using inner alignment when r approaches 0. When r goes to 0, it becomes $3\rho^*_{in}$. Although r can never truly equal zero in a practical design, it can be reduced to nearly zero if the hole pattern incorporates a stronger material such as metal or plastic to reinforce the center island.

4.6 Monte Carlo vs Theoretical

For the 3-blade cases, our derivations are validated by comparing Monte Carlo simulations (MC) to our closed-form expressions (CF) as shown in Fig. 14. The left image, Fig. 14a, shows the two probability density functions side by side for comparison. The two are the nearly identical, verifying our CF results. Fig. 14b shows a zoomed-in view of the bottom 3-blade patterns from Fig. 14a and increases the number of blades in the pattern. It can clearly be seen that the larger the number of blades in the pattern, the less robust it is for handling misalignment. Inspecting Fig. 15 indicates that the 2-blade design has a larger overall area of feasible positions with a higher probability of success than any of the other designs with more than 2 blades.

5 Design Case Study

Design Framework Using Ψ defined in (1), three different design methods can be outlined based on known constraints for a particular application. These can be alignment tolerance Ψ^*, a minimal r based on material properties, or a maximum W based on the size constraints for the mechanism.

The designer must first decide if 2 or 3 blades work better for the application. The 2-blade design has a better Ψ but uses r to align, while 3-blades has a worse Ψ but does not use r for alignment. The flow charts shown in Fig. 16 show the process for picking the best design given 2 of the 3 pa-

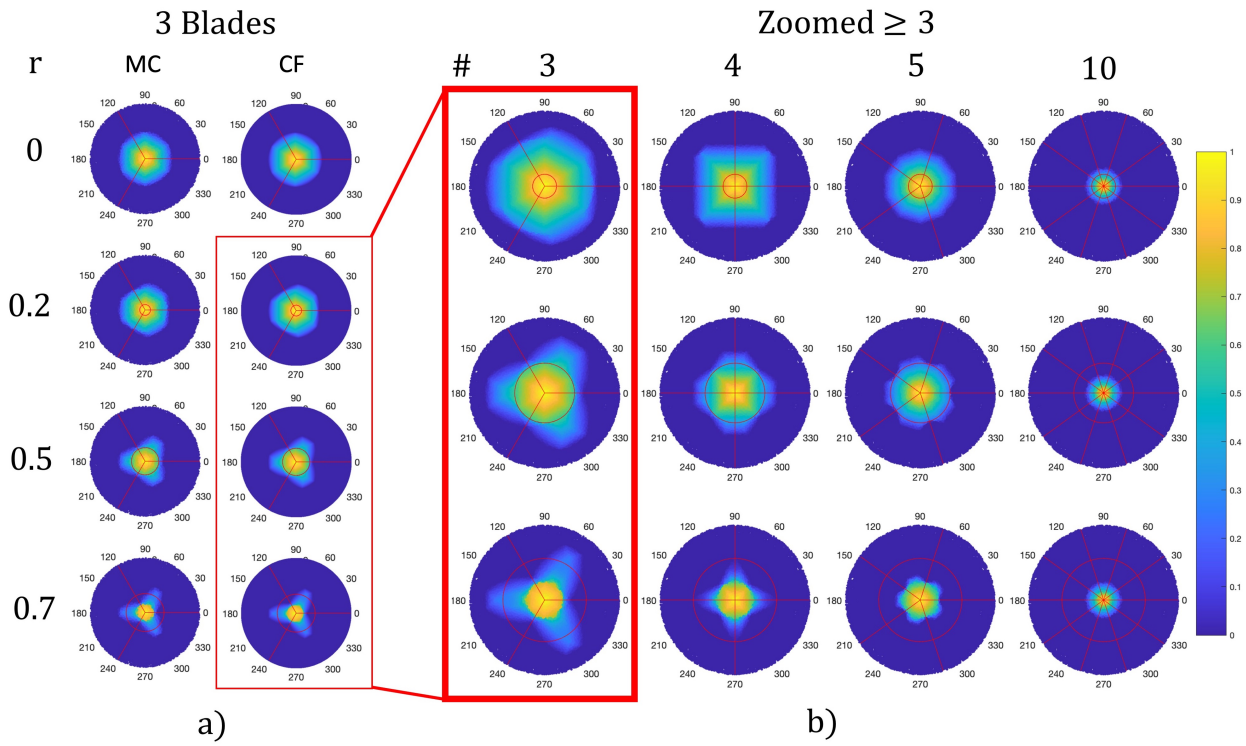

Fig. 14: Depicts p where brighter colors represent higher probabilities of success: a) Monty Carlo (MC) experiments and closed-form (CF) expressions for the 3-blade design, with r values of 0, 0.2, 0.5, and 0.7. b) Zoomed-in figures of our MC experiments for 4, 5, and 10 blades with r values of 0.2, 0.5, and 0.7, where the 3-blade case was added to show how increasing the number of blades decreases the misalignment tolerance.

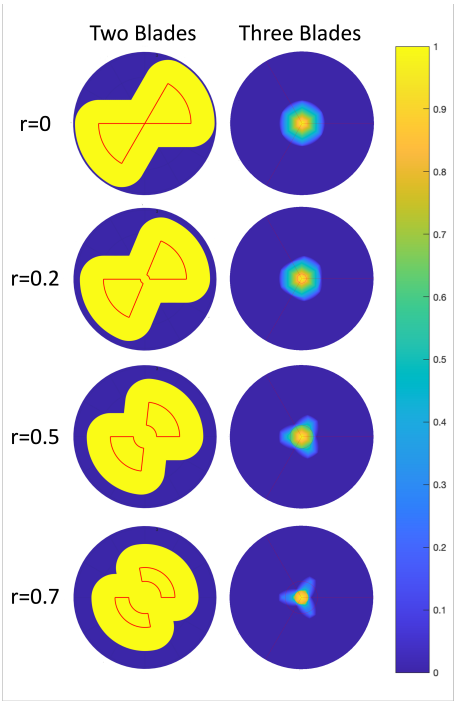

Fig. 15: Varying 2-blade probability distribution on the left versus 3-blade design on the right. As one can clearly see, the 2-blade design is much more robust than the 3-blade design.

rameters. For the 3-blade design, inner align is similar to that of the 2-blade's.

Using Fig. 16a, a viable design for both 2-blade and 3-blade mechanisms for use on LIMMS was developed. We first conducted experiments and determined $r \geq 8$ mm based on the strength of cardboard. Since corrugated cardboard is an orthotropic composite material, patterns were cut with the flutes oriented the same way to eliminate effects from the material anisotropic properties [18].

Verification Experiments To verify the results of our design methodology, both the 2-blade and 3-blade latches were built and tested using two different mating surfaces. The first surface tested was cardboard, which is required for the last mile delivery problem. The cardboard chosen for experiments was C-flute cardboard with a thickness of 4.4 mm, chosen to best simulate the average properties of common shipping boxes. The second surface was acrylic, which is transparent and has a lower coefficient of friction. This was to explore the option of integrating a plastic insert with the cardboard pattern for reinforcement and to study the mechanical behavior of the latch as it rotates. A set of stills from the 2-blade testing on acrylic can be seen in Fig. 17. In this figure, the blue point denotes the center of the hole pattern, and the orange point marks the center of the latch. The red lines indicate the edges of the hole pattern that contact the blades. In Fig. 17a, the hole pattern and the latch are significantly misaligned. As the latch is rotated, the blade tip enters the slot, and the latch self-aligns with the hole pattern.

The blade mechanisms were attached to YORI, a 5-DoF robotic arm [19], to simulate the mechanism's behavior when attached to the LIMMS platform. YORI was operated using a

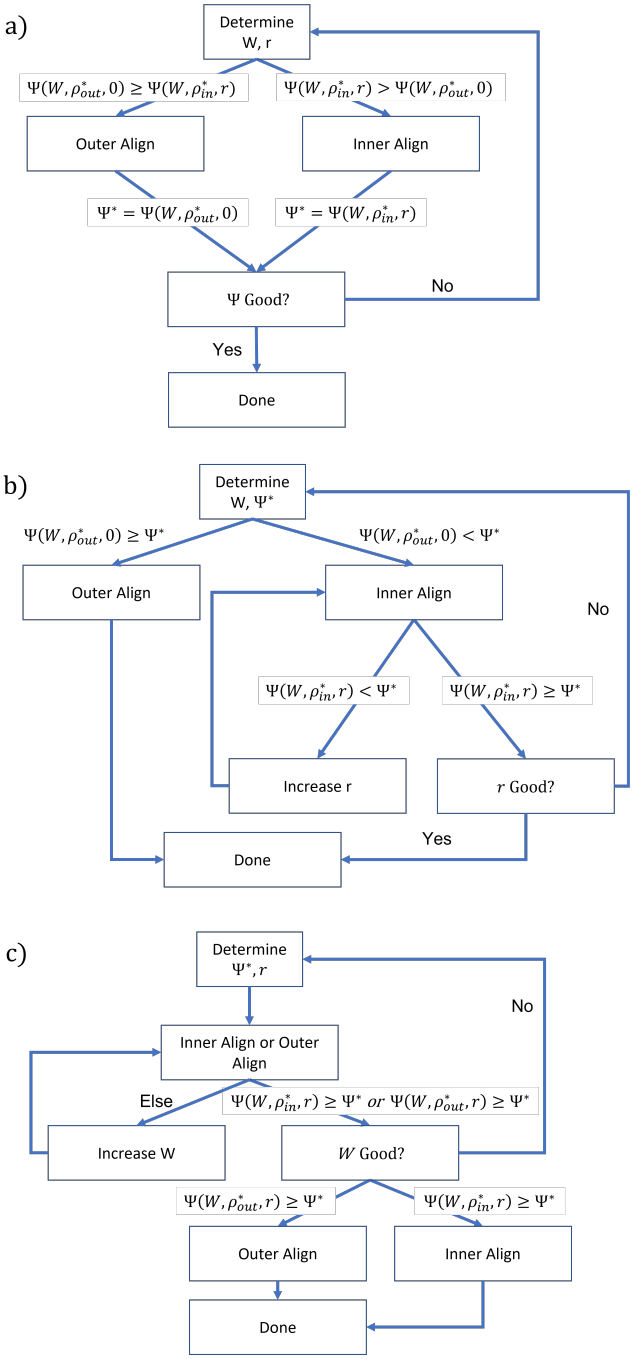

Fig. 16: Design process derived for 3 separate desired design specifications using defined metric Ψ. The process is split based on starting parameters: a) W and r, b) W and Ψ^*, and c) Ψ^* and r.

simple PID (proportional-integral-derivative) controller with minimal gain tuning. In these tests, the latching mechanisms were able to align and hold as expected, as shown in video[1].

Performance Comparison The 2-blade LIMMS latch demonstrated superior alignment capabilities compared to existing latching and alignment methods. While the scale and mechanical approach varies widely between examples, we can still compare alignment performance by designating the connector diameter D_c and connector thickness T_c, and characterize misalignment distance as a ratio of these geometries. The LIMMS prototype latch uses parameters ρ = 35 mm, W = 40 mm, D_c = 80 mm, and T_c = 36 mm from the base to the blade tips.

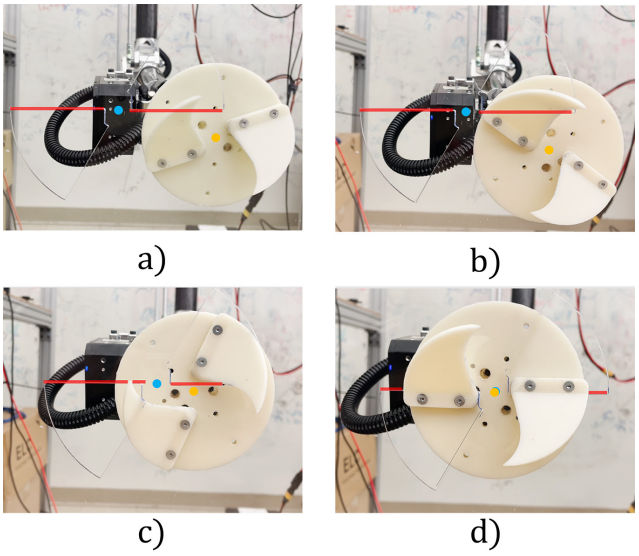

Fig. 17: Two-blade latching with an acrylic mating surface. The blue point is the center of the hole pattern, and the orange point marks the center of the latch. The red lines depict the hole pattern edges that contact the blades.

It is important to note that most existing latching methods use male and female hole patterns with identical diameters. For LIMMS, however, the connector diameter D_c does not connect into a hole pattern of the same diameter. The hole pattern diameter D_h is 140 mm, since the hole pattern on the cardboard does not have the same size constraints as the connector. This significantly increases the area of acceptance for successful latching. Additionally, for the following comparisons, we define displacement in the X or Y direction as parallel to the mating surfaces, while displacement in Z is the perpendicular distance between the mating surfaces.

Most existing literature does not include an analysis of tolerance to misalignment, but the few examples that do can only tolerate a very small amount of misalignment. For example, the HiGen connector, when misaligned in X or Y by $0.035D$, experienced a ∼65% drop in success rate [7]. It also has a tolerance range of $0.33T_c$ in Z with a ∼50% drop in success rate. Comparatively, our data and experiments show that the LIMMS prototype latch can be misaligned by up to $1.31D_c$ and $0.83T_c$ with a 100% success rate. This is a tolerance increase of 37x and 2.5x respectively.

For angular misalignments, the LIMMS latch's capabilities far exceed that of existing latches, with a 100% success rate at any angle about the Z-axis, even when considerably displaced in X-Y. This is thanks to the blade design, which features point contacts that can engage at any location in the slots. By comparison, the HiGen connector experiences a ∼75% drop in success when displaced up to 12°. Other non-radial designs exhibit even lower tolerances, up to 1.7° [13].

As a final note, the latch prototype used in these experiments does not represent the fully optimal case. These performance metrics can be enhanced even further by changing some aspects of the design. The area of acceptance in X-Y could be increased by setting $\rho = W$, which would allow

the blade tips to engage even when displaced by a distance equal to the entire connector diameter. The prototype could reach a theoretical misalignment tolerance of $3\rho^*_{in}$ or $1.5D_c$ with these changes. While not the focus of this paper, tolerance to Z-axis and angular misalignments can be improved by increasing the blade length or angle of attack.

6 Conclusion

In this paper, we analyzed a class of self-aligning rotational latching mechanisms and manufactured prototypes for use on LIMMS. The probability distributions for both 2-blade and 3-blade designs were formally derived and verified using MC and CF. By inspection of Fig. 14, it is clear that the 2-blade design outperforms the others in terms of self-alignment. As the number of blades increased, the rate of success decreased overall. From the probability distribution, a new metric Ψ was introduced to compare relative designs and quantify alignment tolerance. This metric also demonstrated that the 2-blade latching mechanism achieves self-alignment more consistently than the other designs. Depending on the specific application, using both Ψ and the probability distribution may be preferable when designing the latch as there may be subtle trade-offs between robustness in (x, y) and θ. Our analysis also showed that the 2-blade latch can be misaligned as far as $3\rho^*_{in}$ away and still align successfully with the hole pattern.

Our analyses were formalized as a design process for this type of latching mechanism to find optimal design specifications for specific constraints as laid out in Fig. 16. We then used this methodology to manufacture both a 2-blade and 3-blade latching mechanism. The theory was then tested using these mechanisms with a robotic arm holding a single off-center position with PID control. The results of these experiments with two different surface materials were consistent with our theory, and the prototype demonstrated superior alignment capabilities compared to existing methods.

Future Work The theory described in this paper serves as an excellent basis for creating an optimal latch design for the LIMMS system. We will further continue to develop tighter bounds for R^* in the 2-blade inner align design. Nonetheless, the proposed system provides reliable alignment, which is vital for LIMMS as a delivery platform. However, its alignment capabilities could be enhanced even further by exploring more topics, such as, trying to optimize the arcs of the hole pattern such that they do not have to be circular. Most notably, we plan on studying the effects of blade length and angle of attack for better tolerance to Z-axis and angular displacements. Another topic to explore would be the development of a generalized p function for n blades to further study the effects of redundancies and constraints. More practically, we plan on studying the dynamics of these latches in order to develop controllers that use their robustness such that fast latching is possible with minimal damage to the box.

In the immediate future, methods for locking the rotation after torque is no longer being applied will be explored, most likely through an actuated locking mechanism. When fully engaged, the latching pattern itself provides geometries that constrain 5 out of the 6 DoF, and the last degree of freedom (Z-axis rotation) must be fully constrained to form a rigid connection. Since the blades also prevent counter-clockwise rotation in Z, the locking mechanism only needs to prevent clockwise rotation in Z. One option currently being explored is using small *reverse blades* that deploy after successful alignment to prevent clockwise rotation. A worm drive will allow these blades to remain locked in place without supplying continuous power. With these improvements, this mechanically intelligent latching mechanism could allow LIMMS to quickly and reliably perform its operations and enhance mobile delivery operations in the future.

Acknowledgements Special thanks to LG Electronics for sponsoring this research and providing useful feedback.

References

[1] Zhu, T., Fernandez, G., Togashi, C., Liu, Y., and Hong, D., 2022. "Feasibility study of limms, a multi-agent modular robotic delivery system with various locomotion and manipulation modes". In 2022 19th International Conference on Ubiquitous Robots (UR), IEEE.

[2] Gökler, M. I., and Koc, M. B., 1997. "Design of an automatic tool changer with disc magazine for a cnc horizontal machining center". *International Journal of Machine Tools and Manufacture,* **37**(3), pp. 277–286.

[3] Hays, A. B., Tchoryk Jr, P., Pavlich, J. C., Ritter, G. A., and Wassick, G. J., 2004. "Advancements in design of an autonomous satellite docking system". In Spacecraft Platforms and Infrastructure, Vol. 5419, SPIE, pp. 107–118.

[4] Gampe, F., Priesett, K., and Bentall, R., 1985. "A modular docking mechanism for in-orbit assembly and spacecraft servicing". In NASA. Ames Research Center 19th Aerospace Mech. Symp.

[5] Mccown, W., and Bennett, N., 1988. "Structural latches for modular assembly of spacecraft and space mechanisms". In NASA. Langley Research Center, The 22nd Aerospace Mechanisms Symposium.

[6] Sproewitz, A., Billard, A., Dillenbourg, P., and Ijspeert, A. J., 2009. "Roombots-mechanical design of self-reconfiguring modular robots for adaptive furniture". In 2009 IEEE international conference on robotics and automation, IEEE, pp. 4259–4264.

[7] Parrott, C., Dodd, T. J., and Groß, R., 2014. "Higen: A high-speed genderless mechanical connection mechanism with single-sided disconnect for self-reconfigurable modular robots". In 2014 IEEE/RSJ International Conference on Intelligent Robots and Systems, pp. 3926–3932.

[8] Liu, C., Lin, Q., Kim, H., and Yim, M., 2021. "Smores-ep, a modular robot with parallel self-assembly". *arXiv preprint arXiv:2104.00800*.

[9] Murata, S., Yoshida, E., Kamimura, A., Kurokawa, H., Tomita, K., and Kokaji, S., 2002. "M-tran: Self-reconfigurable modular robotic system". *IEEE/ASME transactions on mechatronics,* **7**(4), pp. 431–441.

[10] Yim, M., Duff, D. G., and Roufas, K. D., 2000. "Poly-

bot: a modular reconfigurable robot". In Proceedings 2000 ICRA. Millennium Conference. IEEE International Conference on Robotics and Automation. Symposia Proceedings (Cat. No. 00CH37065), Vol. 1, IEEE, pp. 514–520.

[11] Fukuda, T., Ueyama, T., Kawauchi, Y., and Arai, F., 1992. "Concept of cellular robotic system (cebot) and basic strategies for its realization". *Computers & electrical engineering,* **18**(1), pp. 11–39.

[12] Nilsson, M., 2002. "Heavy-duty connectors for self-reconfiguring robots". In Proceedings 2002 IEEE International Conference on Robotics and Automation (Cat. No. 02CH37292), Vol. 4, IEEE, pp. 4071–4076.

[13] Sproewitz, A., Asadpour, M., Bourquin, Y., and Ijspeert, A. J., 2008. "An active connection mechanism for modular self-reconfigurable robotic systems based on physical latching". In 2008 IEEE International Conference on Robotics and Automation, IEEE, pp. 3508–3513.

[14] Cruijssen, H., Ellenbroek, M., Henderson, M., Petersen, H., Verzijden, P., and Visser, M., 2014. "The european robotic arm: A high-performance mechanism finally on its way to space". In 42nd Aerospace Mechanisms Symposium.

[15] Yip, H. M., Wang, Z., Navarro-Alarcon, D., Li, P., Liu, Y.-h., and Cheung, T. H., 2015. "A new robotic uterine positioner for laparoscopic hysterectomy with passive safety mechanisms: Design and experiments". In 2015 IEEE/RSJ International Conference on Intelligent Robots and Systems (IROS), IEEE, pp. 3188–3194.

[16] Eckenstein, N., and Yim, M., 2012. "The x-face: An improved planar passive mechanical connector for modular self-reconfigurable robots". In 2012 IEEE/RSJ International Conference on Intelligent Robots and Systems, IEEE, pp. 3073–3078.

[17] Fernandez, G. I., Gessow, S., Quan, J., and Hong, D., 2022. "Self-aligning rotational latching mechanisms". In International Design Engineering Technical Conferences and Computers and Information in Engineering Conference, American Society of Mechanical Engineers.

[18] Aboura, Z., Talbi, N., Allaoui, S., and Benzeggagh, M., 2004. "Elastic behavior of corrugated cardboard: experiments and modeling". *Composite structures,* **63**(1), pp. 53–62.

[19] Noh, D., Liu, Y., Rafeedi, F., Nam, H., Gillespie, K., Yi, J.-s., Zhu, T., Xu, Q., and Hong, D., 2020. "Minimal degree of freedom dual-arm manipulation platform with coupling body joint for diverse cooking tasks". In 2020 17th International Conference on Ubiquitous Robots (UR), pp. 225–232.

Appendix

Derivation of the δr and $\delta\vartheta$ Relationship All definitions for angles and side lengths are provided graphically in Fig. 13. We note that $\gamma = \vartheta$ as they form an isosceles triangle with β. Then we can calculate β using $\beta + 2\vartheta = \pi$ and similarly β' using the new triangle defined by $\vartheta + \delta\vartheta$:

$$\beta = \pi - 2\vartheta$$
$$\beta' = \pi - 2(\vartheta + \delta\vartheta) \ .$$

Let $\delta\beta = \beta - \beta'$. Since the red-green-blue triangle is isosceles as both the red side and green side are 2ρ, ω is defined as:

$$\omega = \frac{\pi - \delta\beta}{2} \ .$$

Next δg can be computed using the law of sines:

$$\delta g = sin(\delta\beta)\frac{2\rho}{sin(\omega)} \ .$$

Finally δr can be calculated using the green-black-red triangle and the law of sines:

$$\delta r = \frac{sin(\omega)\delta g}{sin(\pi - (\omega - \gamma) - \omega)} \ ,$$

Where the denominator is the angle opposite $\delta\gamma$ in the green-black-red triangle.

Derivation of δP_l and δP_g The insight for defining δr can be seen in Fig. 13b. If the circle defined by the path of the blade tips passes through δr then the first point will engage such that the second point will also end up in the same cutout, resulting in a Type 2 failure. One example of this is the orange circle with the green points indicating the current and future locations of the blade tips in Fig. 13b. If δr is sufficiently small, this area can be calculated as $\delta r\pi\rho$, which is shown in the shaded region of the figure. At the same time some area is being converted from probability 0 to probability 1 as now a blade tip can reach the upper edge of the cutout removing some Type 0 failures. This area is shown as the yellow sliver sticking out of the probability mass next to the shaded region. This area can be calculated by subtracting two triangles: the smaller one defined by length r and width $r\delta\vartheta$ from the larger one defined by length 2ρ and width $2\rho\delta\vartheta$. This is an upper bound on the area of probability mass added as the yellow sliver sticking out clearly should not have been converted from probability 0 to 1 since it is at least ρ away from δr. δP_l is defined as the probability region that goes from $p = 1$ to $p = 0$.

List of Figures